

MODELING THE INFRARED BOW SHOCK AT δ VELORUM: IMPLICATIONS FOR STUDIES OF DEBRIS DISKS AND λ BOÖTIS STARS

A. GÁSPÁR, K. Y. L. SU, G. H. RIEKE, AND Z. BALOG

Steward Observatory, University of Arizona, Tucson, AZ 85721; agaspar@as.arizona.edu

I. KAMP

Space Telescope Science Division of ESA, STScI, 3700 San Martin Drive, Baltimore, MD 21218

J. R. MARTÍNEZ-GALARZA

Leiden Observatory, Universiteit Leiden, 2300 RA Leiden, The Netherlands

AND

K. STAPELFELDT

Jet Propulsion Laboratory, California Institute of Technology, Pasadena, CA 91109

Received 2007 July 30; accepted 2007 September 9

ABSTRACT

We have discovered a bow shock shaped mid-infrared excess region in front of δ Velorum using 24 μm observations obtained with the Multiband Imaging Photometer for *Spitzer* (MIPS). Although the bow shock morphology was only detected in the 24 μm observations, its excess was also resolved at 70 μm . We show that the stellar heating of an ambient interstellar medium (ISM) cloud can produce the measured flux. Since δ Velorum was classified as a debris disk star previously, our discovery may call into question the same classification of other stars. We model the interaction of the star and ISM, producing images that show the same geometry and surface brightness as is observed. The modeled ISM is ~ 15 times overdense relative to the average Local Bubble value, which is surprising considering the close proximity (24 pc) of δ Velorum. The abundance anomalies of λ Boötis stars have been previously explained as arising from the same type of interaction of stars with the ISM. Low-resolution optical spectra of δ Velorum show that it does not belong to this stellar class. The star therefore is an interesting testbed for the ISM accretion theory of the λ Boötis phenomenon.

Subject headings: infrared: ISM — ISM: kinematics and dynamics — radiation mechanisms: thermal — stars: evolution — stars: imaging — stars: individual (HD 74956, δ Velorum) — shock waves

Online material: color figure

1. INTRODUCTION

Using *IRAS* data, more than a hundred main-sequence stars have been found to have excess emission in the 12–100 μm spectral range (Beckman & Paresce 1993). Many additional examples have been discovered with *ISO* and *Spitzer*. In most cases the spectral energy distributions (SEDs) can be fitted by models of circumstellar debris systems of thermally radiating dust grains with temperatures of 50–200 K. Such grains have short lifetimes around stars: they either get ground down into tiny dust particles that are then ejected by radiation pressure, or if their number density is low they are brought into the star by Poynting-Robertson drag. Since excesses are observed around stars that are much older than the timescale for these clearing mechanisms, it is necessary that the dust be replenished through collisions between planetesimals and the resulting collisional cascades of the products of these events both with themselves and with other bodies. Thus, planetary debris disks are a means to study processes occurring in hundreds of neighboring planetary systems. *Spitzer* observations are revealing a general resemblance in evolutionary timescales and other properties to the events hypothesized to have occurred in the early solar system.

Although the planetary debris disk hypothesis appears to account for a large majority of the far-infrared excesses around main-sequence stars, there are two alternative possibilities. The first is that very hot gas around the stars is responsible for free-free

emission (e.g., Cote 1987; Su et al. 2006). The second possibility is that the excesses arise through heating of dust grains in the interstellar medium around the star, but not in a bound structure such as a debris disk. Kalas et al. (2002) noticed optical reflection nebulosities around a number of stars with Vega-like excesses. These nebulosities show asymmetries that would not be typical of disks, have complex, often striated structures that are reminiscent of the Pleiades reflection nebulosities, and are much too large in extent to be gravitationally bound to the stars (see Gorlova et al. 2006).

Dynamical rather than stationary interactions with the ISM are more interesting (Charbonneau 1991). Originally, it was proposed that ISM dust grains could interact directly with material in debris disks (Lissauer & Griffith 1989; Whitmire et al. 1992). However, it was soon realized that photon pressure from the star would repel interstellar grains, resulting in grain-free zones with possible bow shock geometry around luminous stars (Artymowicz & Clampin 1997).

This scenario has been proposed to account for the abundance anomalies associated with λ Boötis stars. These are late B- to early F-type, Population I stars with surface underabundances of most Fe-peak elements and solar abundances of lighter elements, such as C, N, O, and S. In the diffusion/accretion model (Venn & Lambert 1990; Kamp & Paunzen 2002; Paunzen et al. 2003), it is suggested that the abundance anomaly occurs when a star passes through a diffuse interstellar cloud. The radiation pressure repels

the grains, and hence much of the general ISM metals, while the gas is accreted onto the stellar surface. While the star is within the cloud, a mid-infrared excess will result from the heating of the interstellar dust; however, after the star has left the cloud the abundance anomalies may persist for $\sim 10^6$ yr in its surface layers (Turcotte & Charbonneau 1993) without an accompanying infrared excess.

There have been few opportunities to test the predictions for dynamical interactions of main-sequence stars with the ambient interstellar medium. France et al. (2007) have studied a bow shock generated by the O9.5 runaway star HD 34078. Ueta et al. (2006) describe the bow shock between the mass-loss wind of the AGB star R Hya and the ISM. Noriega-Crespo et al. (1997) identified 58 runaway OB stars with an observable bow shock structure using high resolution *IRAS* 60 μ m emission maps. Rebull et al. (2007) discovered that the young B5 star HD 281159 is interacting with the ISM, producing spherical shells of extended IR emission centered on the star with a spike feature pointing from the star into the shells. None of these cases correspond to the type of situation that might be mistaken for a debris disk, nor which would be expected to produce a λ Boötis abundance pattern.

δ Velorum is a nearby (~ 24 pc) stellar system (at least five members),¹ with modest excess in the *IRAS* data. It has been classified as an A-type star with a debris disk system (e.g., Aumann 1985, 1988; Cote 1987; Chen et al. 2006; Su et al. 2006). Otero et al. (2000) observed a drop in the primary component's brightness (~ 0.3 mag), and showed that it is an eclipsing binary with probably two A spectral-type components. With the available data, Argyle et al. (2002) computed the system's parameters. They suggested that the eclipsing binary (Aa) consists of two A dwarfs with spectral types A1 V and A5 V and masses of 2.7 and 2.0 M_{\odot} and with separation of 10 mas. The nearby B component is a G dwarf with mass around 1 M_{\odot} and separation of 0.6" from the main component. There is also another binary (CD component) at 78" from the star.

In § 2 we report measurements demonstrating that this star is producing a bow shock as it moves through an interstellar cloud as hypothesized by Artymowicz & Clampin (1997). In § 3 we model this behavior using simple dust grain parameters and show satisfactory agreement with expectations for the ISM and properties of the star. We discuss these results in § 4, where we show that the star is most likely not part of the λ Boötis stellar class. Thus, δ Velorum provides a test of the diffusion/accretion hypothesis for λ Boötis behavior.

2. OBSERVATIONS AND DATA REDUCTION

We present observations of δ Velorum at 24 and 70 μ m obtained with the Multiband Imaging Photometer for *Spitzer* (MIPS) as part of three programs: PID 57 (2004 February 21), PID 20296 (2006 February 22, April 3), and PID 30566 (2006 June 12). For PID 57 we used 3 s exposures at four dither positions with a total integration time of 193 s. The other observations at 24 μ m (PID 20296) were done in standard photometry mode with 4 cycles at 5 subpixel-offset cluster positions and 3 s integrations, resulting in a total integration of 902 s on source for each of the two epochs. The star HD 217382 was observed as a point-spread function (PSF) standard (AOR ID 6627584) for PID 57, with the same observational parameters. The observation at 70 μ m (PID 30566) was done in standard photometry default-scale mode with 10 s integrations and 3 cycles, resulting in a total integration of 335 s on source.

¹ It is a complex multiple system: Otero et al. (2000); Hanbury et al. (1974); Horch et al. (2000); Argyle et al. (2002); Tango et al. (1979); Kellerer et al. (2007).

TABLE 1
THE PARAMETERS OF δ VELORUM

Parameter	Value
F_{24}^a	1569 ± 42 mJy
F_{70}^a	237 ± 50 mJy
ρ_{ISM}	$5.8 \pm 0.4 (10^{-24} \text{ g cm}^{-3})$
v_{rel}	$36 \pm 4 \text{ km s}^{-1}$
$F_{\text{star}24}^b$	1277 mJy
$F_{\text{star}70}^b$	147 mJy
$F_{\text{excess}24}^c$	174 mJy
$F_{\text{excess}70}^c$	141 mJy

^a Observed fluxes with the large aperture.

^b Photospheric values, not including G star component.

^c Modeled excesses at large aperture.

The binary component Aa was not in eclipsing phase according to the ephemeris equations by Otero et al. (2000) at either epoch. The period of the eclipse is ~ 45.16 days, and the system was ~ 13 days before a primary minimum at the first, ~ 3 days before one at the second and ~ 7.7 days before one at the third epoch for the 24 μ m observations. The 70 μ m observation was 2.53 days before a secondary minimum.

The data were processed using the MIPS instrument team Data Analysis Tool (DAT; Gordon et al. 2005) as described by Engelbracht et al. (2007) and Gordon et al. (2007). Care was taken to minimize instrumental artifacts (details will be discussed in an upcoming paper, Su et al. 2008, in preparation).

Fitting the model described later demands flux measurements within a constant large external radius (see details in § 3). Therefore, photometry for the target was extracted using aperture photometry with a single aperture setting. The center for the aperture photometry at both 24 and 70 μ m was determined by fitting and centroiding a two-dimensional (2D) Gaussian core. A radius of 56.025" was used for both wavelengths, with sky annulus between 68.95" and 76.34". The aperture size was chosen to be large enough to contain most of the flux from the bow shock, but small enough to exclude the CD component to avoid contamination. The CD component was bright at 24 μ m at a distance of 78" from the AaB components, but could not be detected at 70 μ m. Aperture corrections were not applied because of the large size of the aperture. Conversion factors of 1.068×10^{-3} and 1.652×10^1 mJy arcsec⁻² per MIPS unit were used to transfer measured instrumental units to physical units at 24 and 70 μ m, respectively.

A faint extended asymmetric nebulosity offset from the central star is apparent at 24 μ m, with the dark Airy rings partially filled in. Using standard aperture and PSF fitting photometry optimized for a point source, the total flux is 1420 ± 42 mJy, ~ 1.12 times the expected photospheric flux, which was determined by fitting a Kurucz model (Castelli & Kurucz 2003) to the optical and near-infrared photometry and extrapolating it to 24 and 70 μ m. The large aperture photometry value is greater by another factor of ~ 1.1 , which puts it above the expected photospheric flux by a factor of ~ 1.25 . The final photometry measurements (using the large aperture setting) are listed in Table 1. We also list the modeled photospheric flux of the star and the modeled value of the IR excess. Since the measured excess depends on the aperture used, to avoid confusion we do not give a measured excess value, only the photospheric flux that can be subtracted from any later measurements. The photospheric flux given in Table 1 does not include the contribution from the G dwarf (90 and 10 mJy at 24 and 70 μ m, respectively). The top left panel in Figure 1 shows

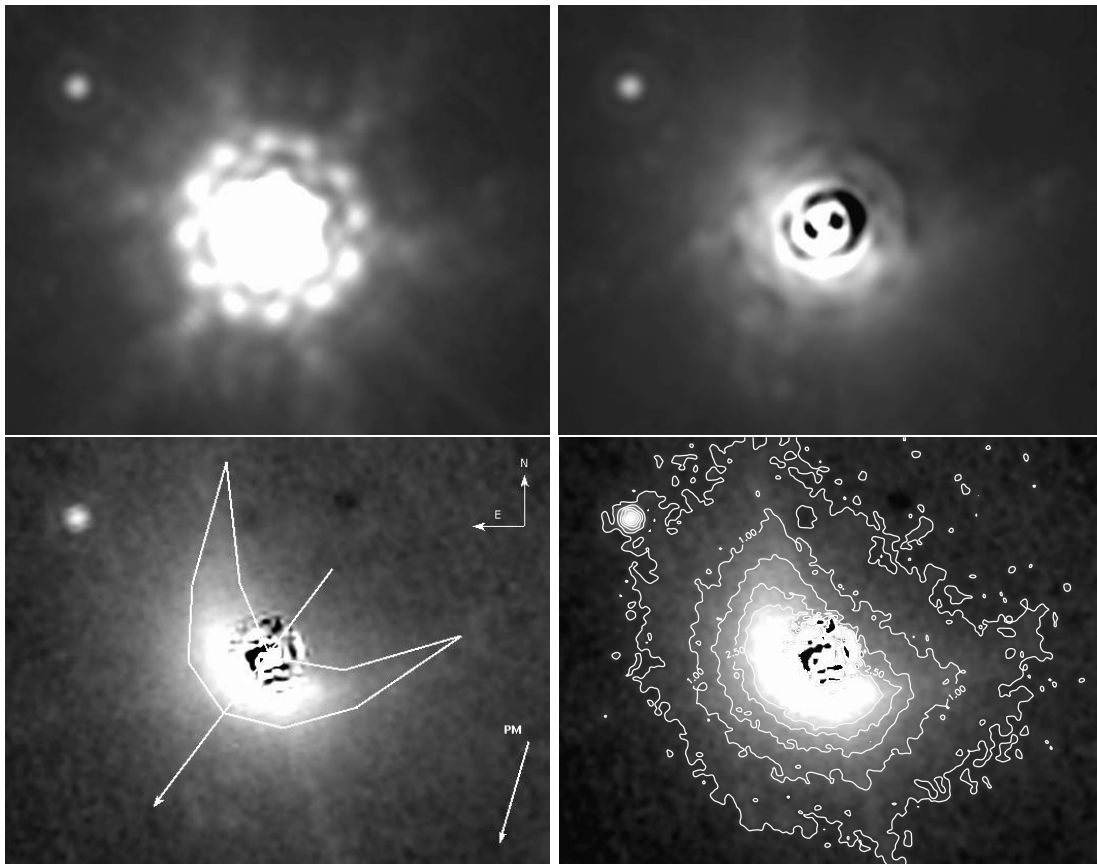


FIG. 1.—Panels show $24\ \mu\text{m}$ images of δ Velorum. All images are in logarithmic scaling. The FOV is $\sim 2.74' \times 2.34'$. The scaling of the images is $-0.5\text{--}4\ \text{MJy sr}^{-1}$. *Top left panel:* The original observed composite image from the second and third epochs. *Top right panel:* PSF oversubtracted image, which shows the bow shock structure far from the star. *Bottom left panel:* The intensity scaled PSF subtracted image (first epoch), which shows the bow shock structure close to the star. This image shows the orientation of the images and the proper motion direction of the star. The arrow bisecting the bow shock contour shows the calculated direction of the modeled relative velocity. *Bottom right panel:* Same image as the bottom left panel, but with intensity contours plotted. The intensity contours are at 0.25, 1.0, 1.75, 2.5, and $3.25\ \text{MJy sr}^{-1}$ from the faintest to the brightest, respectively. The contours show that the extended emission consists of incomplete spherical shells, centered on δ Velorum.

the summed image from epochs 2 and 3, to demonstrate the asymmetry suggested even before PSF subtraction.

For the first epoch $24\ \mu\text{m}$ image, the reference star image was subtracted from the image of δ Velorum, with a scale factor chosen as the maximum value that would completely remove the image core without creating significant negative flux residuals. The deeper exposures from the second and third epochs were designed to reveal faint structures far from the star, where the observed PSF is difficult to extract accurately. Therefore, we used simulated PSFs [from STinyTim (Krist 2002)] and the MIPS simulator.² Because bright structures nearly in the PSF contribute to the residuals at large distances, we oversubtracted the PSF to compensate. The first-epoch PSF-subtracted $24\ \mu\text{m}$ image is shown in the bottom panels of Figure 1 and the composite from epochs 2 and 3 in the upper right.

The PSF-subtracted images in Figure 1 show that the asymmetry is caused by a bow shock. As shown in the lower left, the head of the bow shock points approximately toward the direction of the stellar proper motion. The bottom right panel shows the excess flux contours, and that it consists of incomplete spherical shells centered on δ Velorum. Combined with the upper right image, there is also a parabolic cavity, as expected for a bow shock. The stagnation points (where photon pressure equals gravita-

tional force) of the grains in the bow shock are within ~ 200 AU of the star, according to the observations. A notable feature in the upper right is the wings of the bow shock, which are detectable to ~ 1500 AU.

The $70\ \mu\text{m}$ observation is shown in Figure 2. The PSF subtraction (scaled to the point-source flux of $125\ \text{mJy}$) does not reveal the bow shock structure at this wavelength, only that there is extended excess. The total flux of the residual of the PSF subtracted image is $119\ \text{mJy}$. The intensity contours (*last panel*) suggest that the $70\ \mu\text{m}$ excess fades at the cavity behind the star, but the effect is small. The geometry and direction of the bow shock are discussed in more detail in § 3.2.

3. THE BOW SHOCK MODEL

Based on a previous suggestion by Venn & Lambert (1990), Kamp & Paunzen (2002) proposed a physical model to explain the abundance pattern of λ Boötis stars through star-ISM interaction and the diffusion/accretion hypothesis. Their model is based on a luminous main-sequence star passing through a diffuse ISM cloud. The star blows the interstellar dust grains away by its radiation pressure, but accretes the interstellar gas onto its surface, thus establishing a thin surface layer with abundance anomalies. So long as the star is inside the cloud, the dust grains are heated to produce excess in the infrared above the photospheric radiation of the star. Martínez-Galarza et al. (2008, in preparation) have developed a model of this process and show

² Software designed to simulate MIPS data, including optical distortions, using the same observing templates used in flight.

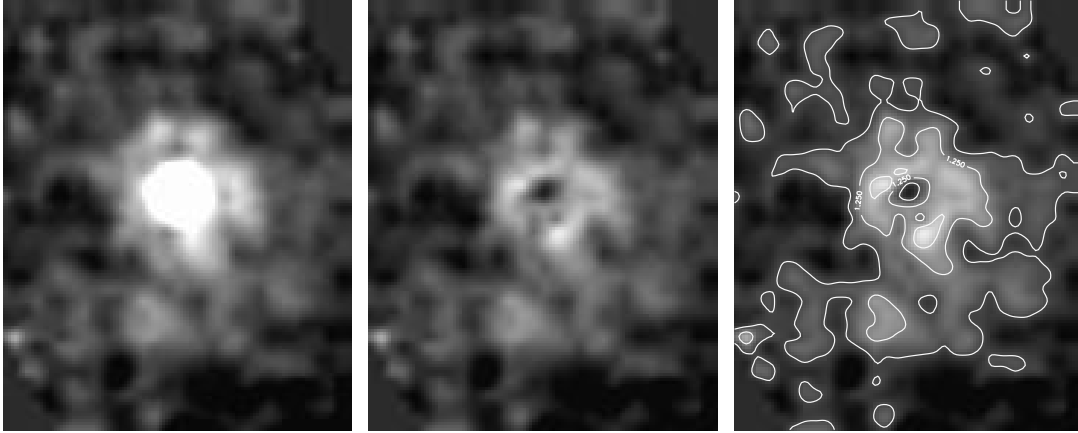


FIG. 2.—Panels show the 70 μm image of δ Velorum. All images are scaled logarithmically from -0.5 to 3 MJy sr^{-1} . The FOV is $\sim 2.46' \times 3.03'$. The orientation of the images is the same as in Fig. 1. *Left*: The observed image. *Middle*: The PSF subtracted image. The residual flux seems close to being concentric. *Right*: The intensity contours. They suggest that there is a faint concentric 70 μm excess further from the star that fades at the cavity region behind the star.

that the global spectral energy distributions of a group of λ Boötis type stars that have infrared excesses are consistent with the emission from the hypothesized ISM cloud. Details of the model can be found in their paper. Here we adapt their model and improve its fidelity (e.g., with higher resolution integrations), and also model the surface brightness distribution to describe the observed bow shock seen around δ Velorum.

3.1. Physical Description of the Model

The phenomenon of star-ISM interactions generating bow shocks was first studied by Artymowicz & Clampin (1997). They showed that the radiative pressure force on a submicron dust grain can be many times that of the gravitational force as it approaches the star. The scattering surface will be a parabola with the star at the focus point of the parabolic shaped dust cavity. Since the star heats the grains outside of the cavity and close to the parabolic surface, an infrared-emitting bow shock feature is expected.

The shape of the parabola (for each grain size) can be given in terms of the distance between the star (focus) and the vertex. This so-called avoidance radius (or the $p/2$ parameter of the scattering parabola) can be calculated from energy conservation to be (Artymowicz & Clampin 1997)

$$r_{\text{av}}^a = \frac{2(\beta^a - 1)MG}{v_{\text{rel}}^2}, \quad (1)$$

where a is the radius of the particle, M is the mass of the star, and v_{rel} is the relative velocity between the star and the dust grains.

The term β^a is the ratio of photon pressure to gravitational force on a grain, and it is given by (Burns et al. 1979)

$$\beta^a = 0.57 Q_{\text{pr}}^a \frac{L/L_{\odot}}{M/M_{\odot}} \left(\frac{a}{\mu\text{m}} \right)^{-1} \left(\frac{\delta}{\text{g cm}^{-3}} \right)^{-1}, \quad (2)$$

where δ is the bulk density of the grain material, and Q_{pr}^a is the radiation pressure efficiency averaged over the stellar spectrum. The term $Q_{\text{pr}}^a(\lambda)$ can be expressed in terms of grain properties [absorption coefficient $Q_{\text{ab}}^a(\lambda)$, scattering coefficient $Q_{\text{sca}}^a(\lambda)$, and the scattering asymmetry factor $g = \langle \cos \alpha(\lambda) \rangle$]; (Burns et al. 1979; Henyey & Greenstein 1938):

$$Q_{\text{pr}}^a(\lambda) = Q_{\text{ab}}^a(\lambda) + Q_{\text{sca}}^a(1 - g), \quad (3)$$

which gives

$$Q_{\text{pr}}^a = \frac{\int Q_{\text{pr}}^a(\lambda) B(T_*, \lambda) d\lambda}{\int B(T_*, \lambda) d\lambda}, \quad (4)$$

where $B(T_*, \lambda)$ is the Planck function. We adopted astronomical silicates in our model with $\delta = 3.3 \text{ g cm}^{-3}$ from Draine & Lee (1984) and Laor & Draine (1993). We considered a MRN (Mathis et al. 1977) grain size distribution in our model:

$$dn = Ca^{-\gamma} da, \quad (5)$$

where C is a scaling constant, and n is the number density of the cloud with $\gamma = 3.5$ and grain sizes ranging from 0.005 to $0.25 \mu\text{m}$.

With these equations we are able to model the avoidance cavity for a grain that encounters a star with known mass, luminosity, and relative velocity. The model describes a situation where the expelled grains are instantly removed from the system rather than drifting away, but this only causes a minor discrepancy in the wing and almost none in the apex of the parabola compared to the actual case. In the actual scenario only those particles get scattered back upstream that encounter the central star with small impact parameter ($\sim r_{\text{av}}^a/2$). This means that most of the grains will get expelled toward the wings, where the grains go further out and emit less infrared excess, and thus their contribution to the total flux will be small.

The model determines the number density of certain grain sizes and the position of their parabolic avoidance cavity. Outside of the cavity we assumed a constant number density distribution for each grain size. To calculate the surface brightness of the system and its SED we assumed a thermal equilibrium condition, with wavelength dependent absorption and an optically thin cloud.

3.2. Model Geometry and Parameters

The model described in § 3.1 gives the distribution and temperature for each grain size. This model was implemented in two ANSI C programs. The first program fits the SED of the system to the observed photometry points, while the second program calculates the surface brightness of the system. The fitted photometry included *uvby*, *UBV*, *Hipparcos V* band, 2MASS, *IRAS*, and MIPS (24 and 70 μm) data. We subtracted the 24 and 70 μm flux contributed by the G star (90 and 10 mJy, respectively) from the MIPS observations, because we wanted to model the system consisting of the two A stars and the bow shock.

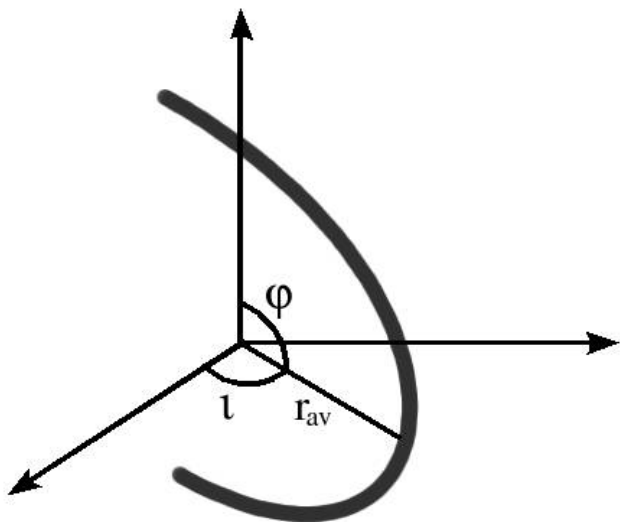


FIG. 3.—Nomenclature of the angles of the system. The heavy line is the grain avoidance parabola. φ is the rotation angle of the system on the plane of the sky (our initial guess was 4° north from the calculated direction of relative motion shown in Fig. 1), ι is the inclination, and r_{av} is an avoidance radius. The observer is viewing from the axis pointing to the bottom left.

The input parameters are: stellar radius, mass-to-luminosity ratio (MLR), relative velocity of cloud and star, ISM dust density, cloud external radius, and the distance of the system. The stellar radius, MLR, and the distance can be constrained easily. We determined the best-fit Kurucz model (Castelli & Kurucz 2003) by fitting the photometry points at wavelengths shorter than $10 \mu\text{m}$. Since the distance is known to high accuracy from *Hipparcos*, we can determine the radius and thus the luminosity of the star precisely. The mass was adopted from Argyle et al. (2002). The G dwarf's luminosity is only 1% of the system, so leaving the star out does not cause any inconsistency. Its mass is only 17% of the total mass, which can only cause minor changes in the determined final relative velocity, but none in the final surface brightness or the computed ISM density. The model then has three variable parameters: the density of the ISM grains (ρ_{dust} ; does not include gas), the relative velocity between the cloud and the star (v_{rel}), and the external radius of the cloud (r_{ext}). The model should describe the total flux from exactly the area used for our photometry. The aperture radius of $56.025''$ (1366 AU at the stellar distance of 24.45 pc) was used as r_{ext} . Both programs calculate the Q_{pr}^a , β^a , r_{av}^a , n values, and then the temperature at r_{av}^a for each grain size.

The SED modeling program decreases the temperature value from the one at r_{av} by 0.01 K steps and finds the radius for that corresponding grain temperature. The program does not include geometrical parameters such as the inclination or the rotation angle of the system, since these are irrelevant in calculating the total flux. It calculates the contribution to the emitting flux for every grain size from every shell to an external radius (r_{ext}) and adds them up according to wavelength.

The program that calculates the surface brightness uses a similar algorithm as the SED program, but it calculates the temperature at 1 AU distance steps from r_{av}^a for every grain size and calculates the total flux in the line of sight in 1 AU² resolution elements.

The total inclination ι of the bow shock was not included as a parameter, since by eye the observed images seemed to show an inclination of $\iota \approx 90^\circ$ (a schematic plot of the angle nomenclature is shown in Fig. 3). This approximation is strengthened by the radial velocity of the star, which is only $\sim 2 \text{ km s}^{-1}$ compared to the tangential velocity of $\sim 13 \text{ km s}^{-1}$. This assures that the motion of the system is close to perpendicular to the line of sight. However, we have found that the bow shock has similar appearance for a significant range of angles ($\pm 20^\circ$) relative to $\iota = 90^\circ$. We illustrate this in Figure 4. If the relative velocity vector had a 70° (or 110°) inclination, it would only cause minor differences in the modeled velocity ($\Delta v_{\text{rel}} \approx 3 \text{ km s}^{-1}$) and ISM density ($\Delta \rho_{\text{ISM}} \approx 0.2 \times 10^{-24} \text{ g cm}^{-3}$). At an inclination of 50° , the “wings” spread out and the bright rim at the apex starts to become thin.

With interstellar Fe II and Mg II measurements, Lallement et al. (1995) showed that the local interstellar cloud (LIC) has a heliocentric velocity of 26 km s^{-1} moving toward the Galactic coordinate $l = 186 \pm 3^\circ$, $b = -16 \pm 3^\circ$. Since δ Velorum is at $l \approx 272^\circ$, $b \approx -7^\circ$, the LIC is also moving perpendicular to our line of sight at the star and in the direction needed to reach a high relative velocity between the star and cloud. Crawford et al. (1998) showed a low-velocity interstellar Ca K line component in the star's spectrum with $v_{\text{helio}} = 1.3 \pm 0.4 \text{ km s}^{-1}$, which also proves that the ISM's motion is perpendicular to our line of sight at δ Velorum. The offset of the proper motion direction of the star from the head direction of the bow shock by a few degrees could be explained by the ISM velocity. A simple vectorial summation of the star and the ISM velocities should give a net motion in the direction of the bow shock.

3.3. Results

We first tried to find the best-fitting SED to the photometry points corresponding to wavelengths larger than $10 \mu\text{m}$ (MIPS,

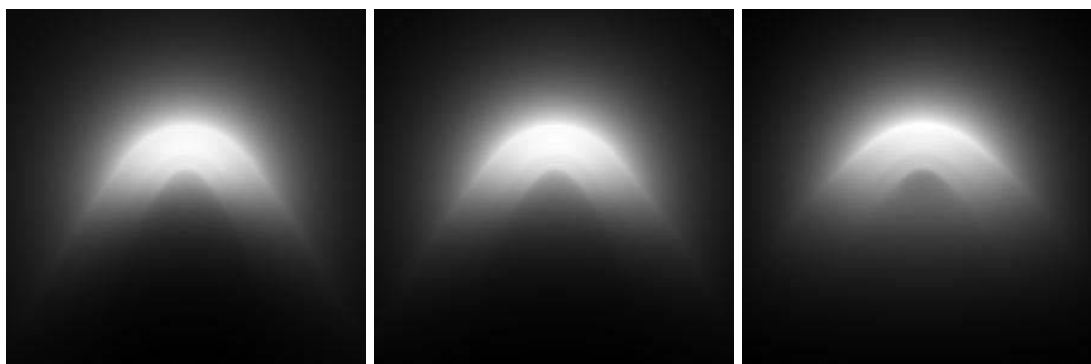


FIG. 4.—Panels show the $24 \mu\text{m}$ morphology of the bow shock viewed at different inclinations, starting from 90° (left), 70° (middle), and 50° (right).

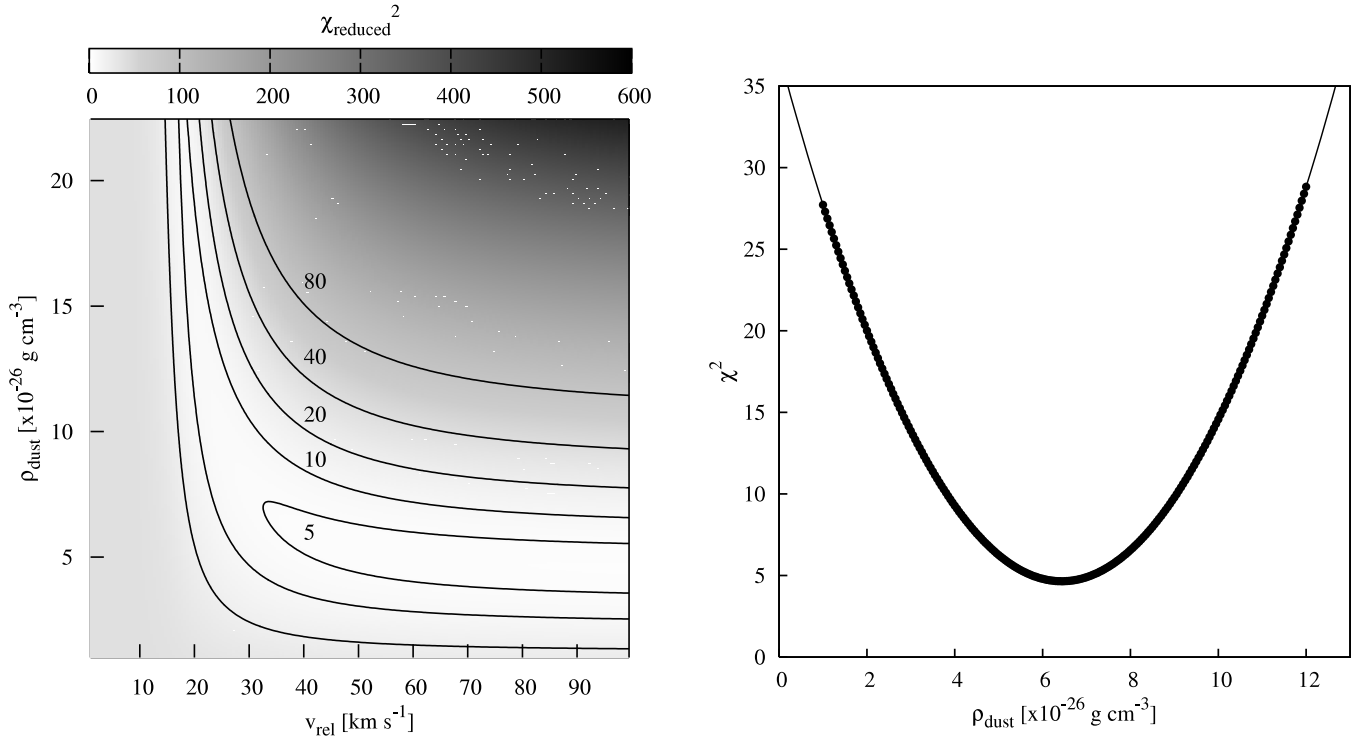


FIG. 5.—*Left:* The χ^2 phase space for ρ_{dust} vs. v_{rel} with constrained $r_{\text{ext}} = 1366$ AU. *Right:* The ρ vs. v_{rel} phase space (*left panel*) cut at $v_{\text{rel}} = 36$ km s $^{-1}$.

IRAS) with χ^2 minimization in the v_{rel} versus ρ_{dust} phase space. We defined χ^2 as

$$\chi^2 = \sum \frac{(F_{\text{obs}} - F_{\text{calc}})^2}{\sigma_{\text{obs}}^2}. \quad (6)$$

The χ^2 phase space with $r_{\text{ext}} = 1366$ AU showed no minimum (Fig. 5, *left panel*). The interpretation of the diagram is as follows: if the relative velocity is small, then the avoidance radius will be large. Consequently, the grains will be at relatively low temperature, and the amount of dust required to produce the observed flux increases. On the other hand, if the relative velocity is large, then the grains can approach closer to the star and heat up to higher temperatures. As a result, a smaller dust density is enough to produce the observed flux. Therefore, the combination of the density of the cloud and the relative velocity can be well constrained by the broadband SED alone, but not each separately.

By using surface brightness values from the observations and the model calculations we were able to determine the v_{rel} parameter and thus eliminate the degeneracy of the model. Since the bow shock is a parabolic feature it has only one variable, the avoidance radius (r_{av}^a), which is the same as the $p/2$ parameter of the parabola (with p being the distance between the focus point and the vertex). The value of r_{av}^a does change as a function of grain size, but the head of the bow shock will be near the value where the avoidance radius has its maximum as a function of grain size. As can be seen in Figure 6, the avoidance radius has a maximum at ~ 0.06 μm grain size. The value of the avoidance radius on the other hand only depends on the relative velocity between the ISM cloud and the star. This way we can constrain the second parameter of the model (v_{rel}). The relative velocity has to be set so that the avoidance radius of the ~ 0.06 μm grain is around half the parabola parameter value. This method gives a

value that only approximates the true one, but it can be used as an initial guess.

The v_{rel} parameter was constrained by comparing the PSF subtracted image “wings” with model images. Within a range of ± 6 km s $^{-1}$ of our initial guess ($v_{\text{rel}} = 35$ km s $^{-1}$) with 1 km s $^{-1}$ steps, we generated images of the surface brightness distribution to a radius of 2500 AU. The computational time for a total $5000 \times 5000 \times 5000$ AU data cube was long, so we only calculated to a depth of 250 AU, keeping the field of view (FOV) 5000×5000 AU. The fluxes of the generated images were normalized (to ensure that the geometry was the main constraint of the fit and not surface brightness variations) and rotated to angles $\varphi = \pm 20^\circ$ with 1° steps. After rotation, both the model images

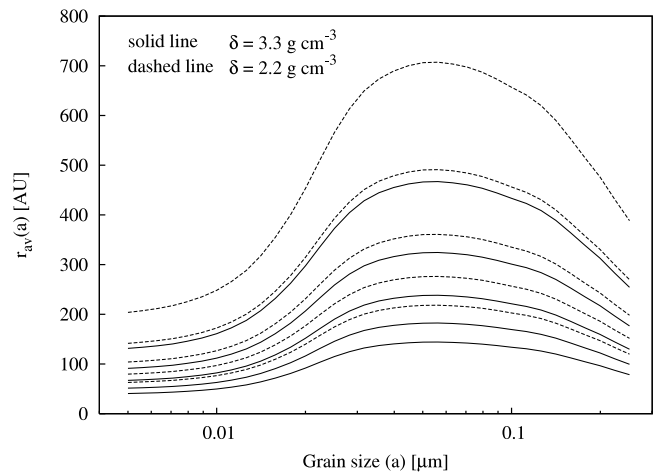


FIG. 6.—Value of r_{av} as a function of grain size. The solid lines are curves for a silicate bulk density of 3.3 g cm $^{-3}$, while the dashed ones are for 2.2 g cm $^{-3}$. The curves are for v_{rel} values of 25 , 30 , 35 , 40 , and 45 km s $^{-1}$ from top to bottom, respectively.

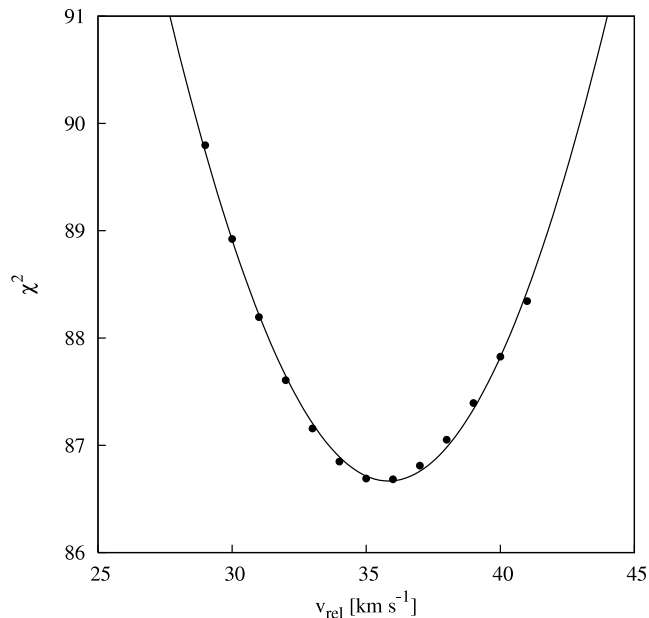
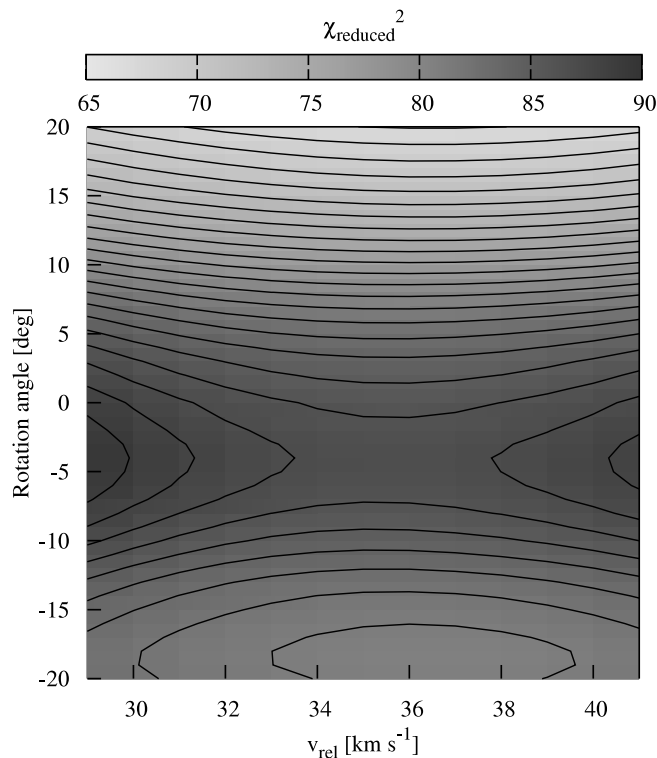


FIG. 7.—*Left panel:* χ^2 in the phase space of φ vs. v_{rel} . *Right panel:* The phase space cut at $\varphi = -4^\circ$, showing the best fit for v_{rel} .

and the observed image were masked with zeros, where there was no detectable surface brightness in the observed image.

The χ^2 of the deviations of the model from the observed image were calculated. We were able to constrain the rotation angle of the model and the relative velocity of the cloud to the star. The χ^2 values in the φ versus v_{rel} phase space are shown in Figure 7 (*left panel*). The small values at large rotation angles are artifacts due to the masking. The best-fit rotation angle is at $\varphi = -4^\circ$ to our initial guess, which means that the direction of motion is 143° counterclockwise (CCW) of north. This is just 21° from the proper motion direction. The ISM velocity predicted from vectorial velocity summation to fit this angle is 24 km s^{-1} , which is close to the ISM velocity value calculated by Lallement et al. (1995). The tangential velocity direction of the ISM from the summation is $\sim 47^\circ$ clockwise (CW) of north, which is pointing only 4.5° south from the Galactic plane.

The v_{rel} parameter and its error are calculated by fitting a Gaussian to the phase space values at $\varphi = -4^\circ$ (Fig. 7, *right panel*). One σ errors are given by values at $\Delta\chi^2 = 1$. The fits give $v_{\text{rel}} = 35.8 \pm 4.0 \text{ km s}^{-1}$. Figure 5 shows that if v_{rel} is constrained, then we can also determine the density of the cloud from simple SED modeling. The vertical cut of Figure 5 (*left panel*) at $v_{\text{rel}} = 36 \text{ km s}^{-1}$ is shown in the right panel of the same figure. The value $\rho_{\text{dust}} = 6.43 \times 10^{-26} \text{ g cm}^{-3}$ is derived from this fit, which gives an original ISM density of $6.43 \times 10^{-24} \text{ g cm}^{-3}$ assuming the usual 1:100 dust-to-gas mass ratio. This ρ_{dust} is an upper estimate of the actual value, since the model computes what density would be needed to give the observed brightness using a r_{ext} radius sphere. Since the line-of-sight distribution of the dust is not cut off at r_{ext} , we used $\rho_{\text{dust}} = 6.43 \times 10^{-26} \text{ g cm}^{-3}$ as an initial guess; a range of density values was explored with model images.

Since the surface brightness scales with the density, only one image had to be computed, which could be scaled afterward with a constant factor. The resultant χ^2 distribution is shown in Figure 8. The calculated best-fitting ISM density is $5.8 \pm 0.4 \times 10^{-24} \text{ g cm}^{-3}$,

assuming the average 1:100 dust-to-gas mass ratio. The error was calculated at $\Delta\chi^2 = 1$. This density ($n \sim 3.5 \text{ atoms cm}^{-3}$) is only moderately higher than the average galactic ISM density ($\sim 1 \text{ atom cm}^{-3}$). The calculated surface brightness images for the three MIPS wavelengths are shown in Figure 9. The closest stagnation point is for the $0.005 \mu\text{m}$ grains at 64 AU, while the farthest is at 227 AU for $0.056 \mu\text{m}$ grains. The temperature coded image in Figure 10 shows the surface brightness temperature of the bow shock (i.e., the temperature of a blackbody, which would give the same surface brightness in the MIPS wavelengths as observed). Table 1 shows good agreement between the model and the measured values.

The original observed images at 24 and $70 \mu\text{m}$ were compared to the model. We generated model images with high resolution

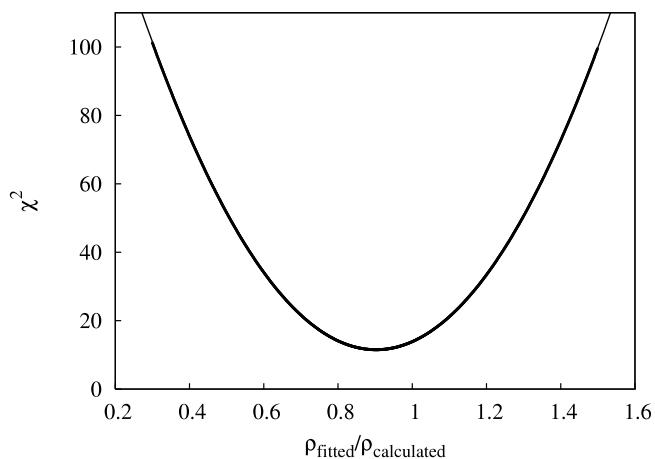


FIG. 8.—Final ISM density was determined from the best-fitting surface brightness image. This plot shows the χ^2 of the fits of the model to the observed image, where $\rho_{\text{calculated}}$ is the initial guess from the right panel of Fig. 5, and ρ_{fitted} is the fitted density using the surface brightness values.

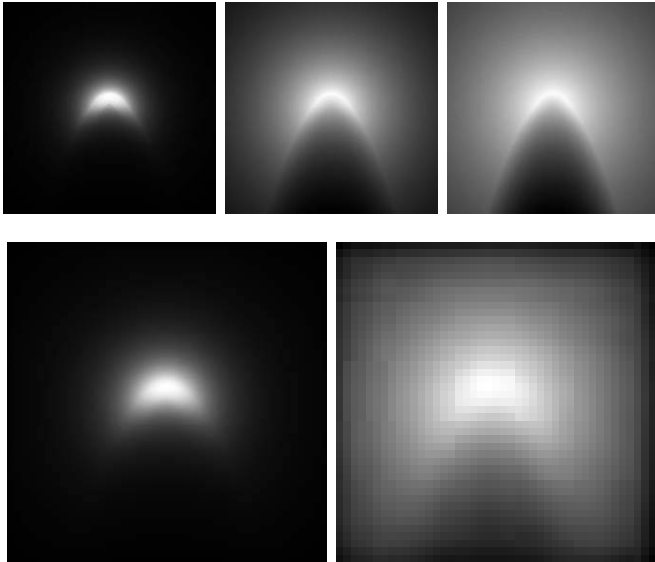


FIG. 9.—*Top panels:* Calculated high resolution surface brightnesses for 24, 70, and 160 μm , respectively. *Bottom panels:* The 24 and 70 μm image with MIPS resolution, convolved with STinyTim PSFs. The images are not rotated to the same angle as the observed bow shock.

that included the bow shock and the central star with its photospheric brightness value at the central pixel. We convolved these images with a 1.8 native pixel boxcar smoothed STinyTim PSF (see Engelbracht et al. 2007). These images were subtracted from the observed ones (Fig. 11). The residuals are small and generally consistent with the expected noise. Finally, the best-fitting SED of the system ($r_{\text{ext}} = 1366$ AU) is plotted in Figure 12. The total mass of the dust inside the $r_{\text{ext}} = 1366$ AU radius is $M_{\text{dust}} = 1.706 \times 10^{24}$ g ($0.023 M_{\text{Moon}}$).

4. DISCUSSION

4.1. Bow Shock Model Results

Our model gives a consistent explanation of the total infrared excess and the surface brightness distribution of the bow shock structure at δ Velorum. The question still remains how common this phenomenon is among the previously identified infrared excess stars. Is it possible that many of the infrared excesses found around early-type stars result from the emission of the ambient ISM cloud? The majority of infrared excess stars are distant and cannot be resolved, so we cannot answer for sure. However, the excess at δ Velorum is relatively warm between 24 and 70 μm [$F(24) \sim 0.17$ Jy, $F(70) \sim 0.14$ Jy], and such behavior may provide an indication of ISM emission. This possibility will be analyzed in a forthcoming paper. Another test would be to search for ISM spectral features. The ISM 9.7 μm silicate feature of the dust grains would have a total flux of ~ 1 mJy for δ Velorum. Since the ~ 1 mJy flux would originate from an extended region and not a point source that could fit in the slit of IRS, it would be nearly impossible to detect with *Spitzer*. Only a faint hint of the excess is visible in the 8 μm IRAC images, consistent with the small output predicted by our model.

4.2. ISM Interactions

To produce a bow shock feature as seen around δ Velorum, the star needs to be luminous, have a rather large relative velocity with respect to the interacting ISM, and be passing through an ISM cloud. A relative velocity of ~ 36 km s^{-1} is not necessarily uncommon, since the ISM in the solar neighborhood has a space

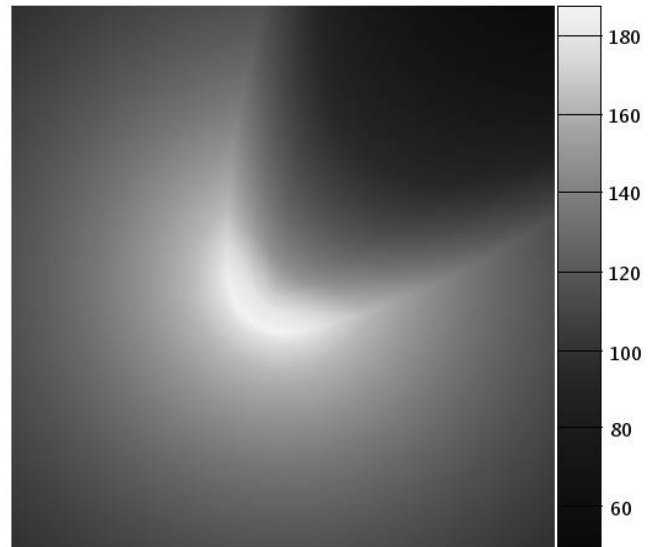


FIG. 10.—Image of the bow shock generated by the model computations. The image's FOV is $2.41' \times 2.41'$. The color scale shows the integrated surface brightness temperature of the bow shock (and not the radial temperature gradient of the grains) in K. [See the electronic edition of the *Journal* for a color version of this figure.]

velocity of ~ 26 km s^{-1} (Lallement et al. 1995), and stars typically move with similar speeds. If the ISM encountering the star is not dense enough the resulting excess will be too faint to be detected. The Sun and its close (~ 100 pc) surroundings are sitting in the Local Bubble [$n(\text{H I}) < 0.24$ cm^{-3} , $T \approx 7500$ K; Lallement 1998; Jenkins 2002]. This cavity generally lacks cold and neutral gas up to ~ 100 pc. The density we calculated at δ Velorum is ~ 15 times higher than the average value inside the Local Bubble. Observations over the past 30 years have shown that this void is not completely deficient of material, but contains filaments and cold clouds (Wennmacher et al. 1992; Herbstmeier & Wennmacher 1998; Jenkins 2002; Meyer et al. 2006). Talbot & Newman (1977) calculated that an average galactic disk star of solar age has probably passed through about 135 clouds of $n(\text{H I}) \geq 10^2$ cm^{-3} and about 16 clouds with $n(\text{H I}) \geq 10^3$ cm^{-3} . Thus the scenario that we propose for δ Velorum is plausible.

4.3. Implications for Diffusion/Accretion Model of λ Boötis Phenomenon

Holweger et al. (1999) list δ Velorum as a simple A star, not a λ Boötis one. We downloaded spectra of the star from the Appalachian State University Nstars Spectra Project (Gray et al. 2006). The spectra of δ Velorum, λ Boötis (prototype of its group), and Vega (an MK A0 standard) are plotted in Figure 13. The metallic lines are generally strong for δ Velorum. One of the most distinctive characteristics of λ Boötis stars is the absence or extreme weakness of the Mg II lines at 4481 \AA (Gray 1988). Although the Mg II line seems to be weaker than expected for an A0 spectral type star, it still shows high abundance, which confirms that δ Velorum is not a λ Boötis type star (Christopher J. Corbally 2007, private communication). The overall metallicity ratio for δ Velorum is $[\text{M}/\text{H}] = -0.33$, while for λ Boötis it is $[\text{M}/\text{H}] = -1.86$ (Gray et al. 2006). The G star's contribution to the total abundance in the spectrum is negligible, because of its relative faintness. We used spectra from the NStars Web site to synthesize a A1 V/A5 V binary composite spectrum and found only minor differences from the A1 V spectrum alone. Thus, the assigned metallicity should be valid.

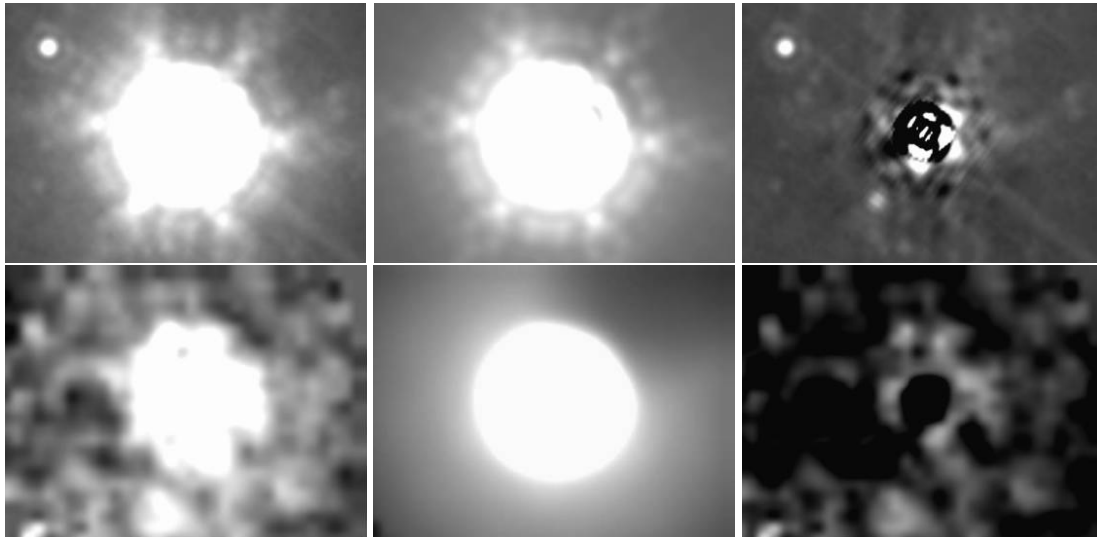


FIG. 11.—*Top row, left panel:* Observed 24 μm image. *Center:* Model 24 μm image including both stellar photosphere and bow shock. *Right:* Model image subtracted from observed. *Bottom row, left panel:* Observed 70 μm image. *Center:* Model 70 μm image including both stellar photosphere and bow shock. *Right:* Model image subtracted from observed. The FOV is $\sim 2.7' \times 2.1'$, north is up and east to the left.

These results show that at δ Velorum, where we do see the ISM interacting with a star, there is no sign of the λ Boötis phenomenon or just a very mild effect. Turcotte & Charbonneau (1993) modeled that an accretion rate of $\sim 10^{-14} M_{\odot} \text{ yr}^{-1}$ is necessary for a $T_{\text{eff}} = 8000$ K main-sequence star to show the spectroscopic characteristics of the phenomenon. The λ Boötis abundance pattern starts to show at $10^{-15} M_{\odot} \text{ yr}^{-1}$ and ceases at $10^{-12} M_{\odot} \text{ yr}^{-1}$. To reach an ISM accretion of $10^{-15} M_{\odot} \text{ yr}^{-1}$, a collecting area of 2 AU radius would be needed with our modeled ISM density and velocity. For an accretion of 10^{-14} , 10^{-13} , and $10^{-12} M_{\odot} \text{ yr}^{-1}$, collecting areas of 6.5, 20, and 65 AU radii are needed, respectively.

With the accretion theory of Bondi & Hoyle (1944), we get an accretion rate of $6.15 \times 10^{-15} M_{\odot} \text{ yr}^{-1}$ for δ Velorum. Thus, the accretion rate for this star is probably not high enough to show a perfect λ Boötis spectrum, but should be high enough for it to show some effects of accretion. This star is an exciting testbed for the diffusion/accretion model of the λ Boötis phenomenon.

5. SUMMARY

We observe a bow shock generated by photon pressure as δ Velorum moves through an interstellar cloud. Although this star was thought to have a debris disk, its infrared excess appears to arise at least in large part from this bow shock. We present a physical model to explain the bow shock. Our calculations reproduce the observed surface brightness of the object and give the physical parameters of the cloud. We determined the density of the surrounding ISM to be $5.8 \pm 0.4 \times 10^{-24} \text{ g cm}^{-3}$. This corresponds to a number density of $n \approx 3.5 \text{ atoms cm}^{-3}$, which means a ~ 15 times overdensity relative to the average Local Bubble value. The cloud and the star have a relative velocity of $35.8 \pm 4.0 \text{ km s}^{-1}$. The velocity of the ISM in the vicinity of δ Velorum we derived is consistent with LIC velocity measurements by Lallement et al. (1995). Our best-fit parameters and measured fluxes are summarized in Table 1.

Holweger et al. (1999) found that δ Velorum is not a λ Boötis star. The measurements from the Nstars Spectra Project also confirm this. Details regarding the diffusion/accretion timescales for a complex stellar system remain to be elaborated. Nevertheless,

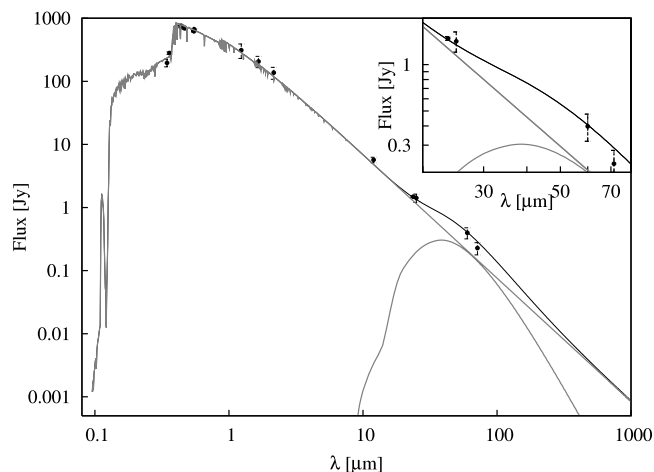


FIG. 12.—Best-fit SED. The window in the upper right corner is a magnified part of the SED between 20 and 80 μm . The plotted fluxes are 24 and 70 μm MIPS and 25 and 60 μm IRAS, with error bars. The 9.7 μm silicate feature in the model SED of the ISM cloud is very faint and on a bright continuum. The flux from the G dwarf has been subtracted from the 24 and 70 μm MIPS observations.

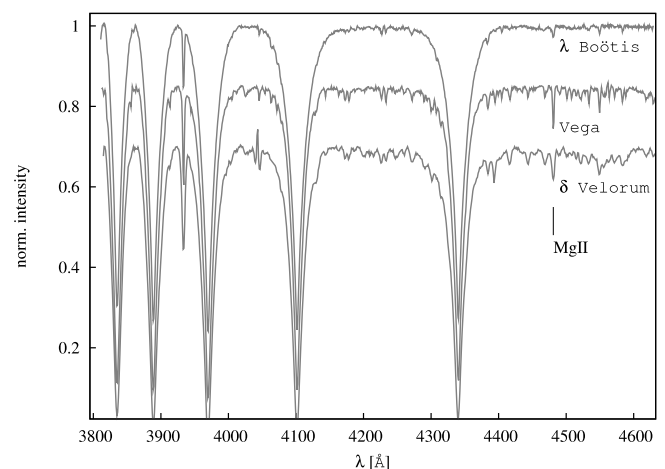


FIG. 13.—Spectra of δ Velorum (*bottom line*), Vega (*middle line*), and λ Boötis (*top line*).

our *Spitzer* observations of δ Velorum provide an interesting test-bed and challenge to the ISM diffusion/accretion theory for the λ Boötis phenomenon.

This work is based on observations with *Spitzer Space Telescope*, which is operated by the Jet Propulsion Laboratory, California Institute of Technology under NASA contract 1407.

Support for this work was provided by NASA through contract 1255094 issued by JPL/Caltech. This research made use of the SIMBAD database, operated at CDS, Strasbourg, France. We would like to thank A. Skemer for help in the error analysis of the model. We have benefited from the helpful discussions with C. Corbally and D. Apai. The analysis of IRAC data by J. Carson helped to confirm our results.

Facilities: Spitzer

REFERENCES

- Argyle, R. W., Alzner, A., & Horch, E. P. 2002, *A&A*, 384, 171
 Artymowicz, P., & Clamplin, M. 1997, *ApJ*, 490, 863
 Aumann, H. H. 1985, *PASP*, 97, 885
 ———. 1988, *AJ*, 96, 1415
 Beckman, D., & Paresce, F. 1993, in *Protostars and Planets III*, ed. E. H. Levy & J. I. Lunine (Tucson: Univ. Arizona Press), 1253
 Bondi, H., & Hoyle, F. 1944, *MNRAS*, 104, 273
 Burns, J. A., Lamy, P. L., & Soter, S. 1979, *Icarus*, 40, 1
 Castelli, F., & Kurucz, R. L. 2003, *Poster Papers, IAU Symp. 210, Modelling of Stellar Atmospheres*, ed. N. Piskunov, W.W. Weiss, & D.F. Gray (San Francisco: ASP), A20
 Charbonneau, P. 1991, *ApJ*, 372, L33
 Chen, C. H., et al. 2006, *ApJS*, 166, 351
 Cote, J. 1987, *A&A*, 181, 77
 Crawford, I. A., Lallement, R., & Welsh, B. Y. 1998, *MNRAS*, 300, 1181
 Draine, B. T., & Lee, H. M. 1984, *ApJ*, 285, 89
 Engelbracht, C. W., et al. 2007, *PASP*, 119, 994
 France, K., McCandliss, S. R., & Lupu, R. E. 2007, *ApJ*, 655, 920
 Gordon, K. D., et al. 2005, *PASP*, 117, 503
 ———. 2007, *PASP*, 119, 1019
 Gorlova, N., Rieke, G. H., Muzerolle, J., Stauffer, J. R., Siegler, N., Young, E. T., & Stansberry, J. H. 2006, *ApJ*, 649, 1028
 Gray, R. O. 1988, *AJ*, 95, 220
 Gray, R. O., Corbally, C. J., Garrison, R. F., McFadden, M. T., Bubar, E. J., McGahee, C. E., O'Donoghue, A. A., & Knox, E. R. 2006, *AJ*, 132, 161
 Hanbury Brown, R., Davis, J., & Allen, L. R. 1974, *MNRAS*, 167, 121
 Henyey, L. G., & Greenstein, J. L. 1938, *ApJ*, 88, 580
 Herbstmeier, U., & Wennmacher, A. 1998, in *IAU Colloq. 166, The Local Bubble and Beyond*, ed. D. Breitschwerdt, M. J. Freyberg, & J. Truemper (New York: Springer), 117
 Holweber, H., Hempel, M., & Kamp, I. 1999, *A&A*, 350, 603
 Horch, E., Franz, O. G., & Ninkov, Z. 2000, *AJ*, 120, 2638
 Jenkins, E. B. 2002, *ApJ*, 580, 938
 Kalas, P., Graham, J. R., Beckwith, S. V. W., Jewitt, D. C., & Lloyd, J. P. 2002, *ApJ*, 567, 999
 Kamp, I., & Paunzen, E. 2002, *MNRAS*, 335, L45
 Kellerer, A., Petr-Gotzens, M. G., Kervella, P., & Coudé Du Foresto, V. 2007, *A&A*, 469, 633
 Krist, J. 2002, *TinyTIM/SIRTF User's Guide* (Pasadena: SSC)
 Lallement, R. 1998, in *IAU Colloq. 166, The Local Bubble and Beyond*, ed. D. Breitschwerdt, M. J. Freyberg, & J. Truemper (New York: Springer), 19
 Lallement, R., Ferlet, R., Lagrange, A. M., Lemoine, M., & Vidal-Madjar, A. 1995, *A&A*, 304, 461
 Laor, A., & Draine, B. T. 1993, *ApJ*, 402, 441
 Lissauer, J. J., & Griffith, C. A. 1989, *ApJ*, 340, 468
 Mathis, J. S., Rimpl, W., & Nordsieck, K. H. 1977, *ApJ*, 217, 425
 Meyer, D. M., Lauroesch, J. T., Heiles, C., Peek, J. E. G., & Engelhom, K. 2006, *ApJ*, 650, L67
 Noriega-Crespo, A., van Buren, D., & Dgani, R. 1997, *AJ*, 113, 780
 Otero, S. A., Fieseler, P. D., & Lloyd, C. 2000, *Inf. Bull. Variable Stars*, 4999, 1
 Paunzen, E., Kamp, I., Weiss, W. W., & Wiesemeyer, H. 2003, *A&A*, 404, 579
 Rebull, L. M., et al. 2007, *ApJS*, 171, 447
 Su, K. Y. L., et al. 2006, *ApJ*, 653, 675
 Talbot, R. J., Jr., & Newman, M. J. 1977, *ApJS*, 34, 295
 Tango, W. J., Davis, J., Thompson, R. J., & Hanbury, R. 1979, *Proc. Astron. Soc. Australia*, 3, 323
 Turcotte, S., & Charbonneau, P. 1993, *ApJ*, 413, 376
 Ueta, T., et al. 2006, *ApJ*, 648, L39
 Venn, K. A., & Lambert, D. L. 1990, *ApJ*, 363, 234
 Wennmacher, A., Lilienthal, D., & Herbstmeier, U. 1992, *A&A*, 261, L9
 Whitmire, D. P., Matese, J. J., & Whitman, P. G. 1992, *ApJ*, 388, 190